The University of Osaka
Institutional Knowledge Archive

Title	Effect of purity on the internal morphology of blisters on aluminum surfaces
Author(s)	Horikawa, Keitaro; Ishii, Akio
Citation	Results in Materials. 2024, 21, p. 100522
Version Type	VoR
URL	https://hdl.handle.net/11094/97797
rights	This article is licensed under a Creative Commons Attribution 4.0 International License.
Note	

The University of Osaka Institutional Knowledge Archive : OUKA

https://ir.library.osaka-u.ac.jp/

The University of Osaka

Results in Materials 21 (2024) 100522

Contents lists available at ScienceDirect

Results in Materials

journal homepage: www.sciencedirect.com/journal/results-in-materials

Effect of purity on the internal morphology of blisters on aluminum surfaces

Keitaro Horikawa *, Akio Ishii

Department of Mechanical Science and Bioengineering, Graduate School of Engineering Science, Osaka University, 1-3, Machikaneyama, Toyonaka, Osaka, 560-8531, Japan

ARTICLE INFO

Keywords:
Hydrogen
Blistering
Aluminum
Purity
Heat treatment

ABSTRACT

This study investigates the effect of purity of aluminum on the morphology of blisters formed on aluminum plates. To this end, aluminum samples with 99 % and 99.99 % purities are prepared, and blisters are generated on the sample surfaces through atmospheric heat treatment. Subsequently, the morphology of blisters on the surface and within the samples are examined using an ion-milling method and field-emission scanning electron microscopy (FE-SEM) with energy-dispersive X-ray spectroscopy. The FE-SEM images reveal that the shape and number density of the blisters vary with the purity of aluminum. The voids under the blisters are spherical when the purity of aluminum is greater than 99.99 % compared to flatter voids when the purity is 99 %. This morphological change is attributed to the local stress caused by neighboring impurity precipitates, and this is theoretically confirmed through Eshelby's ellipsoidal inclusion analysis.

1. Introduction

Blisters are volume defects occurring on the surface of aluminum sheets owing to the incorporation of hydrogen gas during melting and casting processes [1–5]. The blisters that form during melting and casting and subsequently precipitate during solidification are called primary blisters, whereas those that form during post-casting heat treatment are called secondary blisters. From an industrial perspective, blister formation can be suppressed by reducing the hydrogen content below 0.2 ml/100 g Al through degassing during the melting and casting of aluminum [2]. Previous studies have identified several key factors that contribute to hydrogen absorption and blister formation on the surface of aluminum alloy sheets; these include heat treatment conditions [2,4], elemental compositions [6,7], testing atmospheres [8–10], and friction [11–13]. Controlling blister formation is an industrial challenge and is important for the quality management of aluminum sheets; therefore, it is crucial to understand the underlying blister formation mechanisms. Generally, blisters are formed on aluminum sheets when the internal pressure due to the hydrogen molecules within the volume defect exceeds the strength of the material [2]. These blisters often create flattened cavities in the vicinity of surface protrusions. Recently, researchers have revealed that in the case of blisters occurring on commercially available 99.999 % pure aluminum sheets, internal voids exist as spherical cavities deep within the material, several hundred micrometers below the surface, rather than directly beneath the surface [1]. Therefore, the morphology of aluminum blisters may vary depending on the differences in aluminum purity and material strength. Thus, this study aimed to investigate the relationship between internal blister structures and aluminum purity in more detail by forcibly inducing blisters through atmospheric heat treatment and by observing the morphology of blisters on the surface and within the material from a fundamental perspective.

2. Experimental

Aluminum sheet materials with 99 % purity (2 N) and 99.99 % purity (high purity; 4 N) were used as test samples. Both materials were recrystallized after cold rolling and subjected to degassing treatment. The chemical composition of both 2 N and 4 N samples is presented in Table 1. Test samples measuring 14 and 8 mm in length and width, respectively, were machined from the sheets. All samples were subjected to atmospheric heat treatment using a muffle furnace, wherein the samples were heated to 520 °C for over 1 h, followed by subjecting them to the same temperature for 2 h, and finally, cooling them to room temperature in the furnace. The appearance of blisters on the surfaces after the heat treatment was observed using a digital microscope

* Corresponding author.
E-mail address: k.horikawa.es@osaka-u.ac.jp (K. Horikawa).

https://doi.org/10.1016/j.rinma.2023.100522
Received 14 November 2023; Received in revised form 21 December 2023; Accepted 26 December 2023
Available online 24 January 2024
2590-048X/© 2024 The Authors. Published by Elsevier B.V. This is an open access article under the CC BY license (http://creativecommons.org/licenses/by/4.0/).

Table 1
Chemical composition of the aluminum specimens used in this study (mass %).

	Si	Fe	Cu	Mn	Mg	Cr	Zn	Ti	H*	Al
4 N	0.0004	0.00015	0.00001	0.0004	0.00001	0.00019	0.00046	0.00015	0.17	Re.
2 N	0.04	0.07	0.001	0.001	0.001	0.001	0.001	0.010	0.16	Re.

* ml/100 g Al.

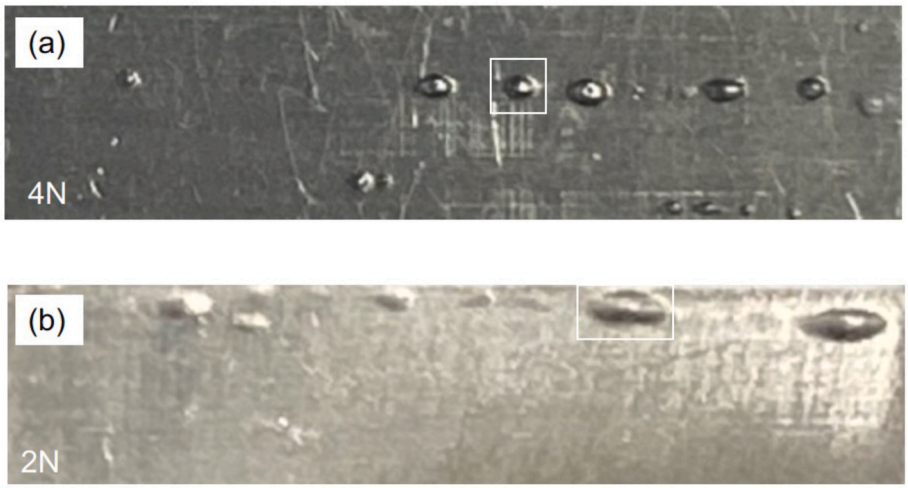

Fig. 1. Examples of blisters generated after the heat treatment, 520 °C for 2h. (a)99.99 % purity aluminum, (b) 99 % purity aluminum. White squares indicate the blisters in both cases which is showing in Fig. 2.

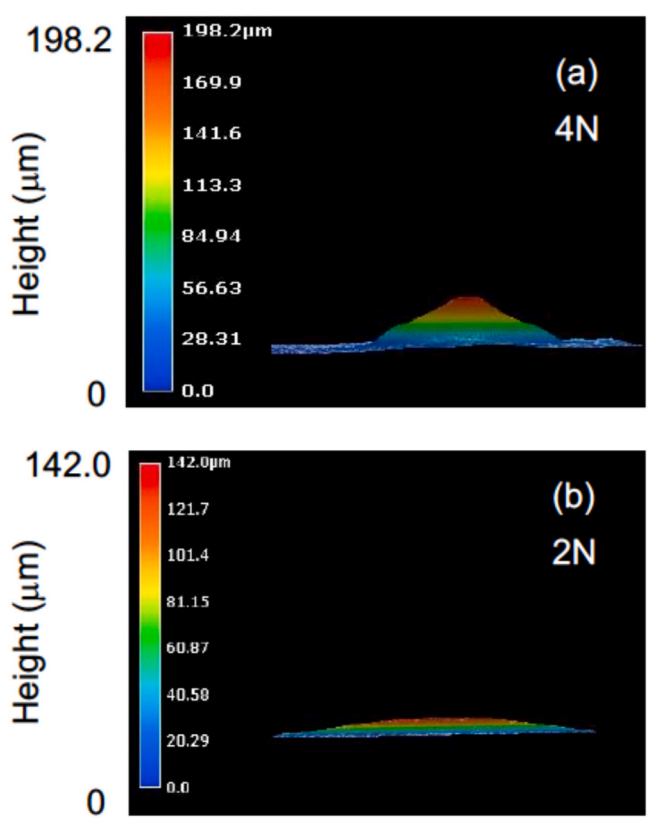

Fig. 2. Side view of blisters generated after the heat treatment, 520 °C for 2h. (a)99.99 % purity aluminum, (b) 99 % purity aluminum.

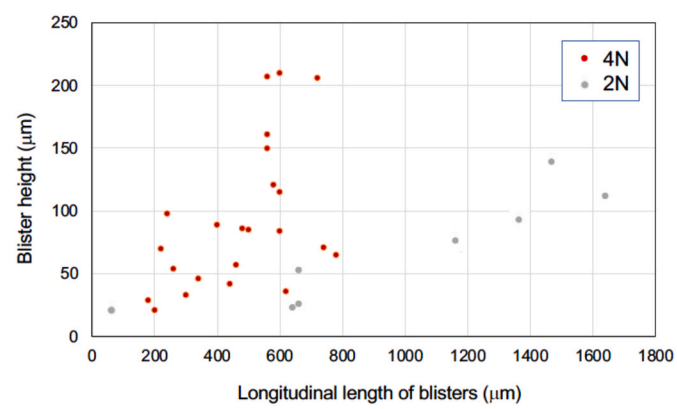

Fig. 3. Relationship between longitudinal length and height of blisters generated in 99.99 % purity (4 N) and 99 % purity (2 N) aluminum.

(Keyence, VW9000). To compare the hydrogen content of the test pieces before and after the heat treatment, temperature-programmed hydrogen desorption analysis (TDA) was conducted using a semiconductor hydrogen sensor-type gas chromatograph (SGHA-P2, FIS). After dry-grinding with emery paper up to #2000, the test pieces were cleaned with acetone (5 min) and dried prior to TDA. TDA was performed on two types of samples: on samples that had not undergone prior heat treatment (as-cast materials) and on samples subjected to heat treatment at 520 °C for 2 h (annealed materials). The heating rate for TDA was 300 °C/h, and the measurement temperature range was from room temperature to 625 °C. To observe the shapes of the defects caused by the blisters on the cross sections of the test samples without applying a load, ion milling was performed using an ion milling apparatus (IM-4000, Hitachi). In the ion milling process, the samples were continuously swung ±30° relative to the ion irradiation direction to create flat surfaces. To avoid deformation of the blister shape during processing, argon ion irradiation was performed from the side of the resin-filled

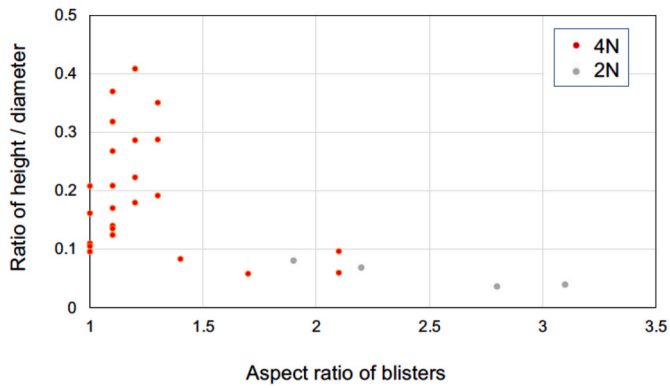

Fig. 4. Relationship between aspect ratio and ratio of height/diameter of blisters generated in 99.99 % purity (4 N) and 99 % purity (2 N) aluminum.

surface where blisters were generated. The blister cross sections were observed using field-emission scanning electron microscopy (FE-SEM, JSM-7600F) with energy-dispersive X-ray spectroscopy (EDX, JED-2300).

3. Results

Fig. 1 shows photographs of the blistered surfaces of 4 N and 2 N aluminum sheets after atmospheric heat treatment at 520 °C for 2 h. Both aluminum sheets are rolled plates, thus the crystal grains elongate in the direction of rolling. It is suggested that blisters also form in the direction of rolling due to the elongation of the microstructure. Fig. 2 presents the surface profiles corresponding to typical blisters formed in each sample. Regarding the shape of the blisters, those formed in 4 N aluminum sheets were mostly circular when viewed from the top and often had a mountain-like shape when viewed from the side. By contrast, the blisters in 2 N aluminum sheets were elliptical when viewed from the top and had smaller variations when viewed from the side. Fig. 3 shows the distribution of the shape of blisters along the blister major axis length (horizontal) with respect to the height of blisters (vertical) for both 2 N and 4 N samples. Evidently, the shapes of the blisters formed in the 2 N samples differed from those in the 4 N samples, as those in the 2 N samples had larger major axis lengths but lower heights compared to those in the 4 N samples.

This finding suggests that a correlation exists between the shapes of the blisters viewed from above and the sides. Considering the shape viewed from above as the aspect ratio AR (major axis: minor axis), and the shape viewed from the side as the height: major axis ratio, the relationship between the shapes can be plotted, as shown in Fig. 4. This figure shows that the distribution of blister shapes can be broadly divided into two groups. Blisters with an aspect ratio smaller than 1.5, especially those with a height: major axis ratio in the range of 0.1–0.4, exhibited mountain-like shapes. When the aspect ratio exceeded 1.5, the blisters became extremely flat with minimal inclination.

Regarding the number of blisters formed, a histogram of the size and frequency of the blisters, approximated as circles on the back and front surfaces of each sample, is shown in Fig. 5. The number of blisters formed in the 2 N samples was lower than that formed in the 4 N samples. Additionally, in the 4 N samples, blisters with sizes below 800 μm were predominant, whereas in the 2 N samples, the blisters size was below 200 μm but some exceeded 1000 μm. This indicates that hydrogen tended to gather at one blister, growing that blister more rapidly in 2 N samples than in 4 N samples. Because the growth of blisters causes cracking, hydrogen embrittlement was more severe in 2 N samples than in 4 N samples.

To confirm the locations of the blisters on the 4 N samples, the surfaces were buff-polished flat after the blister formation, and corrosion tests were performed to expose the grain boundaries for optical microscopy observations. The results are shown in Fig. 6, wherein most of the blisters in the 4 N samples were located at the grain boundaries. The

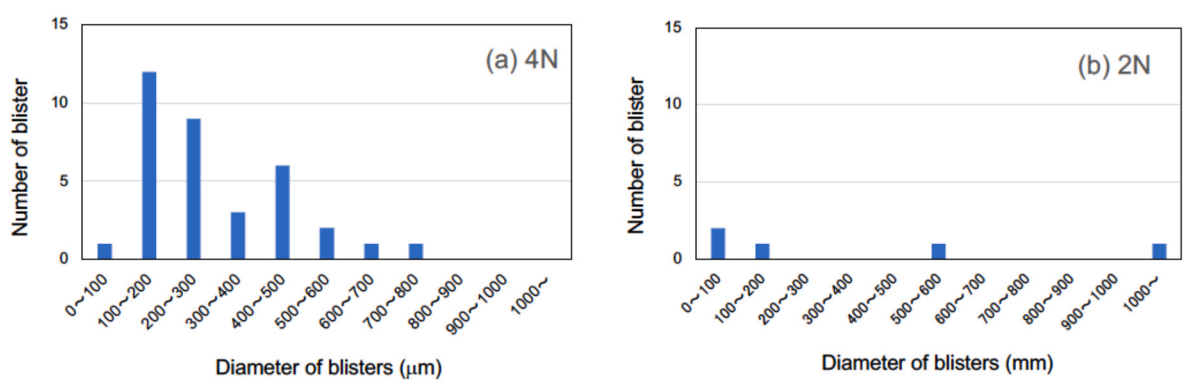

Fig. 5. Number frequency vs. diameter distribution of blisters generated in (a) 99.99 % purity (4 N) and (b) 99 % purity (2 N) aluminum.

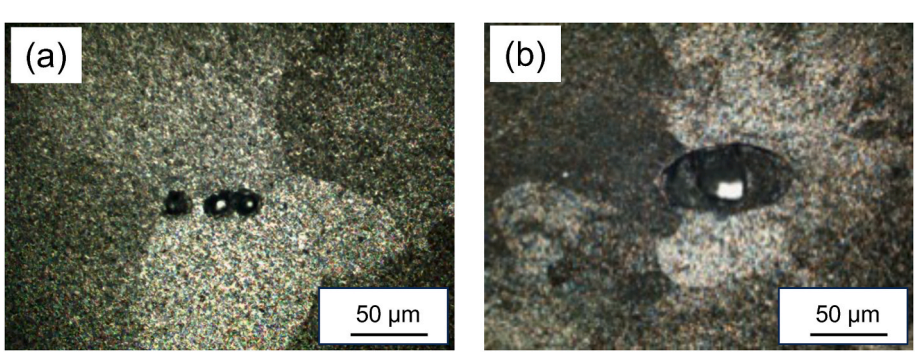

Fig. 6. Appearance of blisters generated at a grain boundary in (a) 99.99 % purity (4 N) and (b) 99 % purity (2 N).

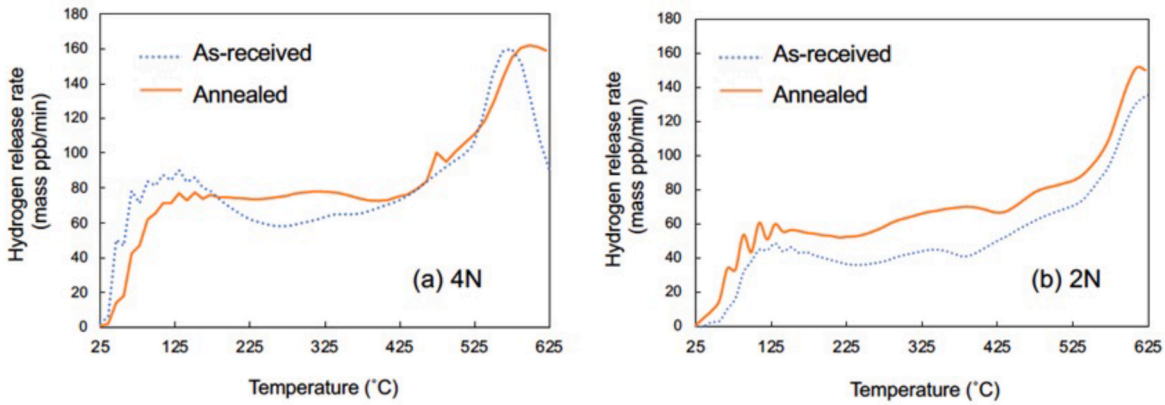

Fig. 7. Thermal hydrogen desorption analysis of (a) 99.99 % purity (4 N) and (b) 99 % purity (2 N) aluminum, as-received or after annealing conditions.

Table 2
Total hydrogen desorption amount determined with TDA.

	As-received (ppm)	Annealed (ppm)	Difference (Annealed-As-received, ppm)
4 N	9.75	9.95	+0.20
2 N	6.18	8.07	+1.90

elongated blisters observed in the 2 N samples also intersect with grain boundaries. Fig. 7 shows the TDA results for the as-received and annealed 2 N and 4 N samples. The total amount of hydrogen released from the samples was determined by calculating the hydrogen release rate over the entire duration of the test, and the results are listed in Table 2. Through heat treatment, both the 4 N and 2 N samples absorbed environmental hydrogen from the moisture content in the annealing atmosphere, resulting in 0.20 mass ppm for the 4 N samples and 1.90 mass ppm for the 2 N samples. Similar to the TDA results reported in previous studies [1] for 5 N aluminum material, the peaks in hydrogen release plots were observed at 125, 325, and above 550 °C. These release patterns are consistent with those reported by a previous study [11]. Based on previous research, each peak corresponds to the release of hydrogen associated with solid-solution hydrogen, dislocations or grain boundaries, and molecular hydrogen.

To examine the morphology of the blisters, two blisters were randomly selected from the 4 N and 2 N samples, and cross-sectional observations were made. The SEM images of the cross-section of blisters in the 4 N samples are shown in Fig. 8, whereas the observation results of blisters that occurred in the 2 N samples are shown in Fig. 9. In one 4 N sample, (blister 1, shown in Fig. 8(a)), a spherical cavity was observed at a depth of 184 μm from the surface of the blister protrusion.

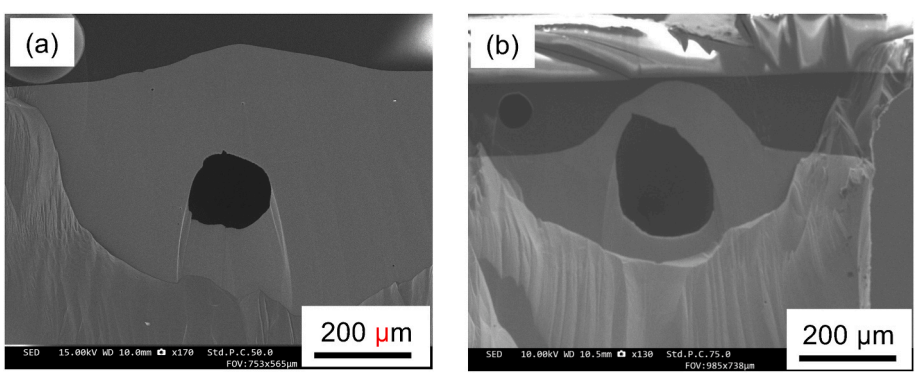

Fig. 8. SEM micrographs showing cross sectional views of two different blisters in 99.99 % purity (4 N), (a) Blister 1, (b) Blister 2.

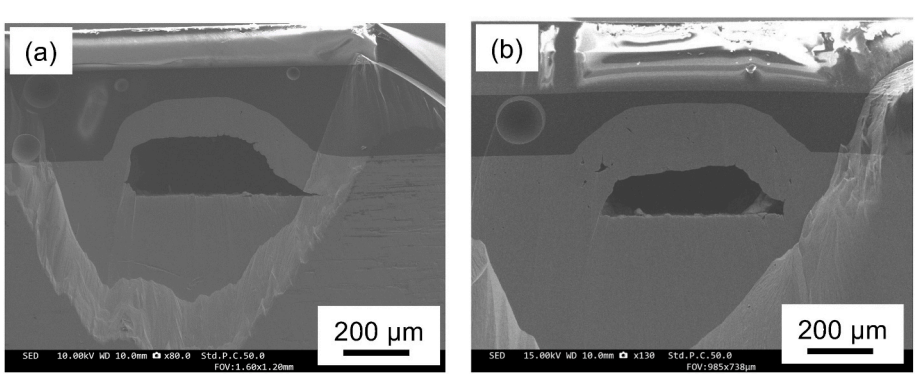

Fig. 9. SEM micrographs showing cross sectional views of two different blisters in 99 % purity (2 N), (a) Blister 1, (b) Blister 2.

Table 3
Location of porosity generated in 99.99 % purity aluminum (4 N) and 99 % purity aluminum (2 N).

	Radius of porosity, r (μm)	Distance from the surface, d (μm)	d/r
4 N ①	65	184	2.83
4 N ②	108	108	1.00
2 N ①	301	136	0.45
2 N ②	205	149	0.72

However, in the other 4 N sample (blister 2, shown in Fig. 8(b)), a spherical cavity was observed at a depth of 100 μm from the surface. The shallower cavity exhibited a change in shape, with the upper part transitioning into a pointed balloon-like shape, as opposed to a perfect sphere.

However, in one 2 N sample (blister 1, shown in Fig. 9(a)), a flat and elongated cavity was observed at a depth of 136 μm from the surface of the blister protrusion. For the other 2 N sample (blister 2, shown in Fig. 9 (b)), a similar flat and elongated cavity was observed at a depth of 149 μm from the surface. In both cases, the cavities had flat bottoms. According to previous studies [3,4], in aluminum alloys, flat cavities exist at a shallow depth of approximately 30 μm from the surface. In the case of ultra-high purity aluminum (99.9997 % purity; 5 N), spherical cavities exist at a depth of approximately 300 μm from the surface [1].

4. Discussion

4.1. 4-1 internal pressure inside blisters

In this study, as the purity decreased from 4 N to 2 N, and the material strength increased, there was a tendency for the position of the cavities to become closer to the surface, and the blister morphology transitioned from spherical to flat. The differences in the morphologies of the blisters between the 2 N and 4 N samples might have been influenced by the stress state around the blisters. When the blister had a flat plate-like shape, the stress acting on the upper layer of metal σ^F can be expressed using the following equation theoretically [14]:

$$\sigma^F = P\left(1 + 0.75\left(\frac{r}{d}\right)^2\right). \tag{1}$$

However, when the blister is spherical, the stress acting on the upper layer of the metal can be expressed as follows [14]:

$$\sigma^F = \frac{3}{2}P\left(1 - \left(\frac{r}{r+d}\right)^3\right)^{-1}, . \tag{2}$$

where r is the radius (half width) of the blister, d is the thickness of the upper metal layer, and P is the pressure inside the blister. Based on the relationship between $\frac{d}{r}$ and $\frac{P}{\sigma^F}$ derived from these equations, it is possible to predict the morphology of the blisters [14]. Based on the observed blister cross sections (Figs. 8 and 9), the values for the radius (r) and thickness of the upper metal layer (d) were used to calculate the parameter $\frac{d}{r}$, as shown in Table 3. For one blister on the 4 N sample (Fig. 8(a)), $\frac{d}{r}$ was greater than 1.1. At this size and location, spherical blisters were more likely to grow, which agreed with the actual observation of spherical blisters in this case. For one blister on the 2 N sample (Fig. 9(a)), $\frac{d}{r}$ was less than 1.1. This condition favored the growth of flat plate-like blisters, which was consistent with the observed morphology. However, in one blister on the 2 N sample (Fig. 8(b)), $\frac{d}{r}$ was less than 1.1, suggesting that spherical blisters were favored by stress conditions. Nevertheless, the observed shape was balloon-like. Thus, although non-negligible agreement exists between theoretical predictions and experimental observations, the difference in the morphology of blisters between 2 N and 4 N may not be fully explained by the difference in material strength between 2 N and 4 N.

Using the yield stress obtained from tensile tests at room temperature and 520 °C (Table 4) as σ^F, the internal pressure P of blisters occurring in the 4 N and 2 N samples was calculated using equations (1) and (2). Assuming that the gas inside the blisters was composed only of hydrogen, the amount of hydrogen inside the cavities C_H, the number of moles of hydrogen (hydrogen concentration inside the blister) were calculated using the following ideal gas state equation (3):

Table 4
Tensile properties of aluminum tested at 520 °C.

	Yield stress (MPa)	Tensile strength (MPa)	Fracture strain
4 N	8.0	9.0	0.76
2 N	10.5	13.4	0.69

Table 5
Pressure and hydrogen concentration inside porosity generated in 99.99 % purity aluminum (4 N) and 99 % purity aluminum (2 N).

	Pressure inside porosity, P (MPa)	Hydrogen concentration inside porosity, CH (mol)
4 N ①	5.24	9.4 × 10-10
4 N ②	4.66	3.7 × 10-9
2 N ①	2.23	1.9 × 10-8
2 N ②	4.33	1.1 × 10-8

$$PV = C_H RT, \tag{3}$$

where V is the blister volume, R is the gas constant, and T is the absolute temperature.

R = 8.31 × 10^3 Pa L/(mol·K) and T = 793 K is used to calculate C_H. The volume inside the blisters was calculated by assuming that the 2 N sample was hemispherical, whereas the 4 N sample was spherical. The results obtained from the calculation using from equations (1)–(3) are summarized in Table 5. The pressure inside the blisters ranged from 2.23 MPa to 5.24 MPa, and no significant difference was observed in internal pressure due to the difference in purity. However, the amount of hydrogen present inside the blisters was estimated to be approximately two orders of magnitude lower in 2 N sample compared to that of 4 N sample.

4.2. 4-2 Eshelby's ellipsoidal inclusion analysis

Considering the previous studies revealed that the shape of hydrogen blisters is correlated with the microstructure of the materials [15,16] and that the normal stress affects the hydrogen concentration [17], another possible explanation for the impurity-dependent morphology change of blisters is that the blisters tend to nucleate around the precipitates of impurities and the local stress caused by the neighboring precipitates affects the shape of the blisters; the plate-like blisters grow under the local stress condition of the impure precipitates in low-purity 2 N samples and the spherical-shaped blisters grow under stress-free conditions without impure precipitates in high-purity 4 N, and vice versa. In the following, we theoretically confirm our assertion using Eshelby's ellipsoidal inclusion theory.

To confirm the above assertion from our experimental observation that the morphology change of the hydrogen blister is because of the local stress caused by the precipitates of the impurity in the Al matrix, we implemented theoretical Eshelby's ellipsoidal inclusion analysis, considering both hydrogen blisters and the precipitates of the impurity in Al matrix as ellipsoidal inclusion ($\frac{x_1^2}{a_1^2} + \frac{x_2^2}{a_2^2} + \frac{x_3^2}{a_3^2} = 1$; $\boldsymbol{x} = [x_1; x_2; x_3]$ indicates the position in Al matrix and a_i $(i = 1, 2, 3)$ is half axis of ellipsoid). Here, let us briefly introduce our method; for details, please refer to pioneering studies by Mura et al. and our recent reports [18–21].

Based on Eshelby's equivalent inclusion theory [22,23], the local stress inside the inclusion, $\sigma_{ij}^{\mathrm{inc}}$, misfit strain of the inclusion, ϵ_{ij}, and Eshelby's fictitious misfit strain, $\widetilde{\epsilon}_{ij}$, have the following relationship using Einstein summation convention,

$$\sigma_{ij}^{\mathrm{inc}} = C_{ijkl}^{\mathrm{mat}}\left(S_{klmn}\widetilde{\epsilon}_{mn} + \varepsilon_{kl}^{0} - \widetilde{\epsilon}_{kl}\right) = C_{ijkl}^{\mathrm{inc}}\left(S_{klmn}\widetilde{\epsilon}_{mn} + \varepsilon_{kl}^{0} - \epsilon_{kl}\right) \tag{4}$$

where C_{ijkl}^{mat} and C_{ijkl}^{inc} are the elastic constants of the matrix and inclusion, respectively. S_{klmn} is the so-called Eshelby's tensor and ε_{kl}^{0} is the environmental strain around the inclusion. The elastic energy increment, ΔE, because of the existence of the inclusion in the matrix (per unit volume of the inclusion) is described using $\sigma_{ij}^{\mathrm{inc}}$, ϵ_{ij} and $\widetilde{\epsilon}_{ij}$, as follows:

$$\Delta E = -\frac{1}{2}\sigma_{ij}^{\mathrm{inc}}\epsilon_{ij} - \sigma_{ij}^{0}\epsilon_{ij} - \frac{1}{2}\sigma_{ij}^{0}\left(\widetilde{\epsilon}_{ij} - \epsilon_{ij}\right). \tag{5}$$

where σ_{ij}^{0} is environmental stress around the inclusion due to ε_{kl}^{0}. In this study, the hydrogen blisters are considered as the ellipsoidal inclusions with very small elastic constant $C_{ijkl}^{\mathrm{inc}} \approx 0$ and $\sigma_{ij}^{\mathrm{inc}} = P\delta_{ij}$ (δ_{ij} is Kronecker delta and P is the hydrogen gas pressure inside the blister in the previous section) [24]. Subsequently, for given C_{ijkl}^{mat}, which is the elastic constant of Al matrix, the aspect ratio of ellipsoidal hydrogen blister $\frac{a_3}{a_1}$ (fixing $a_1 = a_2$) is changed, mimicking the sphere $\left(\frac{a_3}{a_1} = 1\right)$ and plate-like $\left(\frac{a_3}{a_1} \approx 0\right)$ blisters, and $\Delta E\left(\frac{a_3}{a_1}\right)$ is calculated under the certain ε_{kl}^{0} condition, which is caused by the neighboring precipitates of impurity, to find the optimal aspect ratio of hydrogen blister with the minimum ΔE using equations (4) and (5). More concretely, using equation (4), $\widetilde{\epsilon}_{kl}$ is derived first using $\sigma_{ij}^{\mathrm{inc}} = C_{ijkl}^{\mathrm{mat}}(S_{klmn}\widetilde{\epsilon}_{mn} + \varepsilon_{kl}^{0} - \widetilde{\epsilon}_{kl})$ and then the corresponding misfit strain ϵ_{kl} is derived using $\sigma_{ij}^{\mathrm{inc}} = C_{ijkl}^{\mathrm{inc}}(S_{klmn}\widetilde{\epsilon}_{mn} + \varepsilon_{kl}^{0} - \epsilon_{kl})$. With $\sigma_{ij}^{\mathrm{inc}}$, derived ϵ_{ij} and $\widetilde{\epsilon}_{ij}$, ΔE is calculated using equation (2). S_{klmn} in equations (4) and (5) is numerically calculated by the following integration using only C_{ijkl}^{mat} [18,20,25]:

$$S_{klmn} = \frac{1}{8\pi}C_{pqmn}^{\mathrm{mat}}\int_{-1}^{1} d\zeta_3 \int_{0}^{2\pi}\left(\frac{\xi_l\xi_q N_{kp}(\xi_1,\xi_2,\xi_3) + \xi_k\xi_q N_{lp}(\xi_1,\xi_2,\xi_3)}{D(\xi_1,\xi_2,\xi_3)}\right)d\theta \tag{6}$$

where

$$D(\xi_1,\xi_2,\xi_3) = P_{pqr}\left(C_{pj1l}^{\mathrm{mat}}\xi_j\xi_l\right)\left(C_{qm2n}^{\mathrm{mat}}\xi_m\xi_n\right)\left(C_{rs3t}^{\mathrm{mat}}\xi_s\xi_t\right)$$

and

$$N_{km}(\xi_1,\xi_2,\xi_3) = \frac{1}{2}P_{kst}P_{mnr}\left(C_{sjnl}^{\mathrm{mat}}\xi_j\xi_l\right)\left(C_{turv}^{\mathrm{mat}}\xi_u\xi_v\right)$$

correspond to the determinant and cofactor of $K_{km} = C_{klmn}^{\mathrm{mat}}\xi_l\xi_n$, respectively. P_{pqr} denotes the permutation tensor. Using ζ_3 and θ, $\boldsymbol{\xi} = [\xi_1;\ \xi_2;\ \xi_3]$ can be described as

$$\begin{bmatrix}\xi_1\\ \xi_2\\ \xi_3\end{bmatrix} = \begin{bmatrix}\dfrac{\sqrt{1-\zeta_3^2}\cos\theta}{a_1}\\ \dfrac{\sqrt{1-\zeta_3^2}\sin\theta}{a_2}\\ \dfrac{\zeta_3}{a_3}\end{bmatrix}.$$

To determine ε_{ij}^{0} and σ_{ij}^{0} in equations (4) and (5), local stress field around the precipitates is also numerically calculated using the following integration considering the precipitates as ellipsoidal inclusion [19,21],

$$\frac{\partial u_i}{\partial x_j} = C_{klmn}^{\mathrm{mat}}\widetilde{\epsilon}_{mn}\int_{-1}^{1} d\zeta_3 \int_{0}^{2\pi}\left(\frac{\xi_j\xi_l N_{ik}(\xi_1,\xi_2,\xi_3)}{D(\xi_1,\xi_2,\xi_3)}\left(\frac{1}{4\pi}U(\boldsymbol{x}\cdot\boldsymbol{\xi}-1) - \frac{1}{2\pi\widetilde{x}}\delta(\boldsymbol{x}\cdot\boldsymbol{\xi}-1)\right)\right)d\theta \tag{7}$$

$$U(x) = \begin{cases}1\ (x \le 0)\\ 0\ (x > 0)\end{cases},$$

$$\delta(x) = \begin{cases}1\ (x = 0)\\ 0\ (otherwise)\end{cases},$$

$$\widetilde{x} = \sqrt{\left(\frac{x_1}{a_1}\right)^2 + \left(\frac{x_2}{a_2}\right)^2 + \left(\frac{x_3}{a_3}\right)^2}$$

The center of the inclusion is defined as $\boldsymbol{x} = [0;\ 0;\ 0]$ in this equation. The strain and stress fields around the precipitate can be derived as follows:

$$\varepsilon_{ij}(\boldsymbol{x}) = \frac{1}{2}\left(\frac{\partial u_i}{\partial x_j} + \frac{\partial u_j}{\partial x_i}\right)$$

$$\sigma_{ij}(\boldsymbol{x}) = C_{ijkl}^{\mathrm{mat}}\varepsilon_{kl}$$

After calculating $\varepsilon_{ij}(\boldsymbol{x})$ and $\sigma_{ij}(\boldsymbol{x})$, the values of ε_{ij} and σ_{ij} at the vicinity of the precipitates are chosen as ε_{ij}^{0} and σ_{ij}^{0}, respectively, mimicking the hydrogen blister nucleates around the precipitates. Notably, $\widetilde{\epsilon}_{mn}$ in above equation is derived using equation (4) with given misfit strain, ϵ_{kl}, and elastic constant, C_{ijkl}^{inc}, of the precipitates.

For the detailed calculation setting, experimentally observed $P =$ 5.24 and 2.23 MPa (Table 5) are utilized to find optimal blister shape for 4 N and 2 N cases, respectively. An isotropic form is assumed for the elastic constants of the hydrogen blisters.

$$C_{ijkl}^{\mathrm{inc}}\ (for\ hydrogen\ blister) = \lambda\delta_{ij}\delta_{kl} + \mu\left(\delta_{ik}\delta_{jl} + \delta_{il}\delta_{jk}\right),$$

where $\lambda = 0.06$ and $\mu = 0.04$ GPa are used as $C_{ijkl}^{\mathrm{inc}} \approx 0$. Notably, these parameters are confirmed to be robust: $\lambda = 0.006$ and $\mu = 0.004$ GPa produces almost the same results. For the elastic constants of the Al matrix C_{ijkl}^{mat}, the following values for cubic Al (in the conventional coordinate system $[100]_{\mathrm{Al}} - [010]_{\mathrm{Al}} - [001]_{\mathrm{Al}}$) are used, which are calculated using density functional theory (DFT) atomistic simulation, referring to the material project [26]: $C_{1111}^{\mathrm{mat}} (= C_{2222}^{\mathrm{mat}} = C_{3333}^{\mathrm{mat}}) = 104$ GPa, $C_{1122}^{\mathrm{mat}} (= C_{1133}^{\mathrm{mat}} = C_{2233}^{\mathrm{mat}}) = 73$ GPa, and $C_{2323}^{\mathrm{mat}} (= C_{3131}^{\mathrm{mat}} = C_{1212}^{\mathrm{mat}}) = 32$ GPa. Owing to the tensor symmetry, elastic constants generally have the following relationship: $C_{ijkl} = C_{jikl} = C_{ijlk} = C_{klij}$. As a precipitate to calculate the local strain (or stress) field from the composition of the impurity 2 N, the experimentally observed eutectic $(111)_{\mathrm{Al}}$ normal plate-like diamond Si [27,28] is employed in the coordinate system $\boldsymbol{x_1} - \boldsymbol{x_2} - \boldsymbol{x_3} = [1\bar{1}0]_{\mathrm{Al}} - [11\bar{2}]_{\mathrm{Al}} - [111]_{\mathrm{Al}}$, mimicked by a penny ellipsoid ($a_1 = a_2 = 1, a_3 = 0.1$). The following value (in conventional coordinate system $[100]_{\mathrm{Si}} - [010]_{\mathrm{Si}} - [001]_{\mathrm{Si}}$) are used for the cubic elastic constants of Si precipitates, which are also DFT calculated in material project [26]: $C_{1111}^{\mathrm{inc}} (= C_{2222}^{\mathrm{inc}} = C_{3333}^{\mathrm{inc}}) = 144$ GPa, $C_{1122}^{\mathrm{inc}} (= C_{1133}^{\mathrm{inc}} = C_{2233}^{\mathrm{inc}}) = 53$ GPa and $C_{2323}^{\mathrm{inc}} (= C_{3131}^{\mathrm{inc}} = C_{1212}^{\mathrm{inc}}) = 75$ GPa. The cube–cube orientation correspondence between the Al matrix and Si precipitates is assumed based on previous experimental observations [29]. $\epsilon_{ii} = 0.017, \epsilon_{ij} = 0.0\ (i \neq j)$ misfit strains are used, which were estimated for Si precipitates in Al matrix in recent atomistic study [28]. Once we calculated the stress field around plate-like Si, fixing $a_1 = a_2 = 1$ of ellipsoidal hydrogen blister, the aspect ratio of hydrogen blister $\frac{a_3}{a_1}$ is varied from 0.1 (plate-like) to 2 (capsule-like) per 0.1 and ΔE is calculated for each aspect ratio to find the minimum ΔE under ε_{kl}^{0} (or σ_{ij}^{0}) condition owing to the stress field of plate-like Si for 2 N and strain (or stress) free condition for high purity 4 N. Determining a unit for the

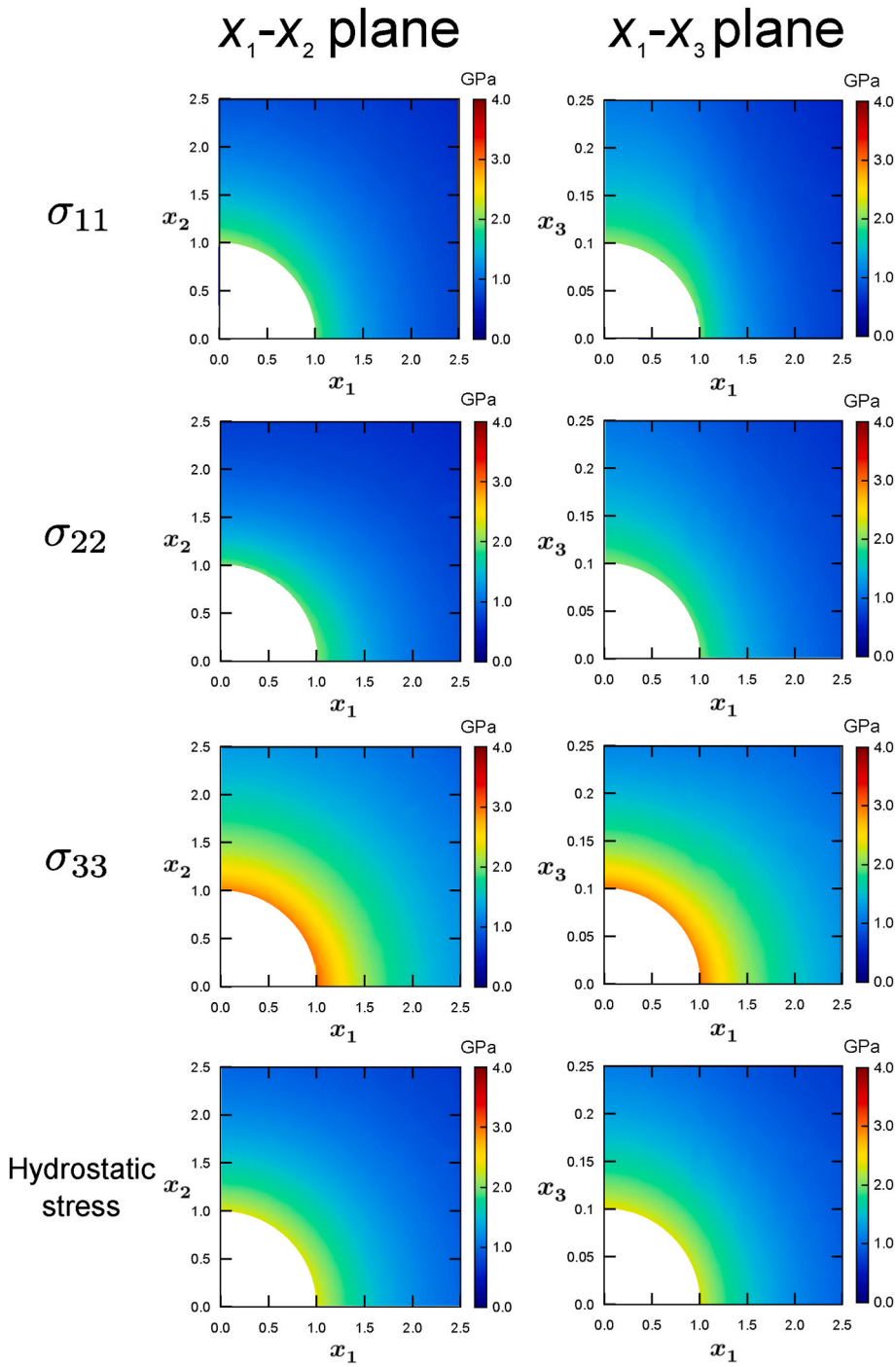

Fig. 10. Local stress fields around the plate-like Si precipitate. Notably, $\sigma_{23}(\boldsymbol{x}) = \sigma_{31}(\boldsymbol{x}) = \sigma_{12}(\boldsymbol{x}) = 0$. The stress fields inside the ellipsoid are omitted.

half-axes is unnecessary because Eshelby's tensor is independent of the inclusion volume. Therefore, the positions in this study are unitless. The stress field is only calculated in the first quadrants of $\boldsymbol{x_1} - \boldsymbol{x_2}$ and $\boldsymbol{x_1} - \boldsymbol{x_3}$ planes by setting the center of the ellipsoidal inclusion at the origin of $\boldsymbol{x}$ coordinate system, considering the symmetry of the ellipsoids. The coordinate conversion of the above elastic constants from $[100]_{\mathrm{Al}} - [010]_{\mathrm{Al}} - [001]_{\mathrm{Al}}$ to $[1\bar{1}0]_{\mathrm{Al}} - [11\bar{2}]_{\mathrm{Al}} - [111]_{\mathrm{Al}}$ is implemented before a series of Eshelby's inclusion analyses using a rotation matrix.

In Fig. 10, the calculated local stress field around the plate-like Si precipitates is shown. Several GPa stress exists around the precipitates and especially, the stress level of σ_{33} component, at the edges of the plate, is quite high, around 4 GPa. This is not only due to the high misfit strain of the Si precipitates, but also the shape of Si (plate-like) and the high elastic constants of Si compared with the Al matrix. In Fig. 11, the aspect ratio $\frac{a_3}{a_1}\left(=\frac{a_3}{a_2}\right)$ of ellipsoidal hydrogen blister vs ΔE plot is shown for the 4 N and 2 N Al cases. As mentioned above, the 4 N blister nucleation under strain (or stress)-free conditions are considered and the 2 N blister nucleates under certain local strain (or stress) conditions because of the impurity precipitates. The plot for 2 N in Fig. 11 is calculated using the strain and stress values at $(x_1, x_2, x_3) = (1.1, 0, 0)$ in Fig. 10 as ε_{ij}^0 and σ_{ij}^0 in equations (1) and (2), assuming the nucleation of blister occurs at the vicinity of a pre-existing Si precipitate. Although the spherical shape $\left(\frac{a_3}{a_1} = 1\right)$ is the favorite for 4 N blister, which has the

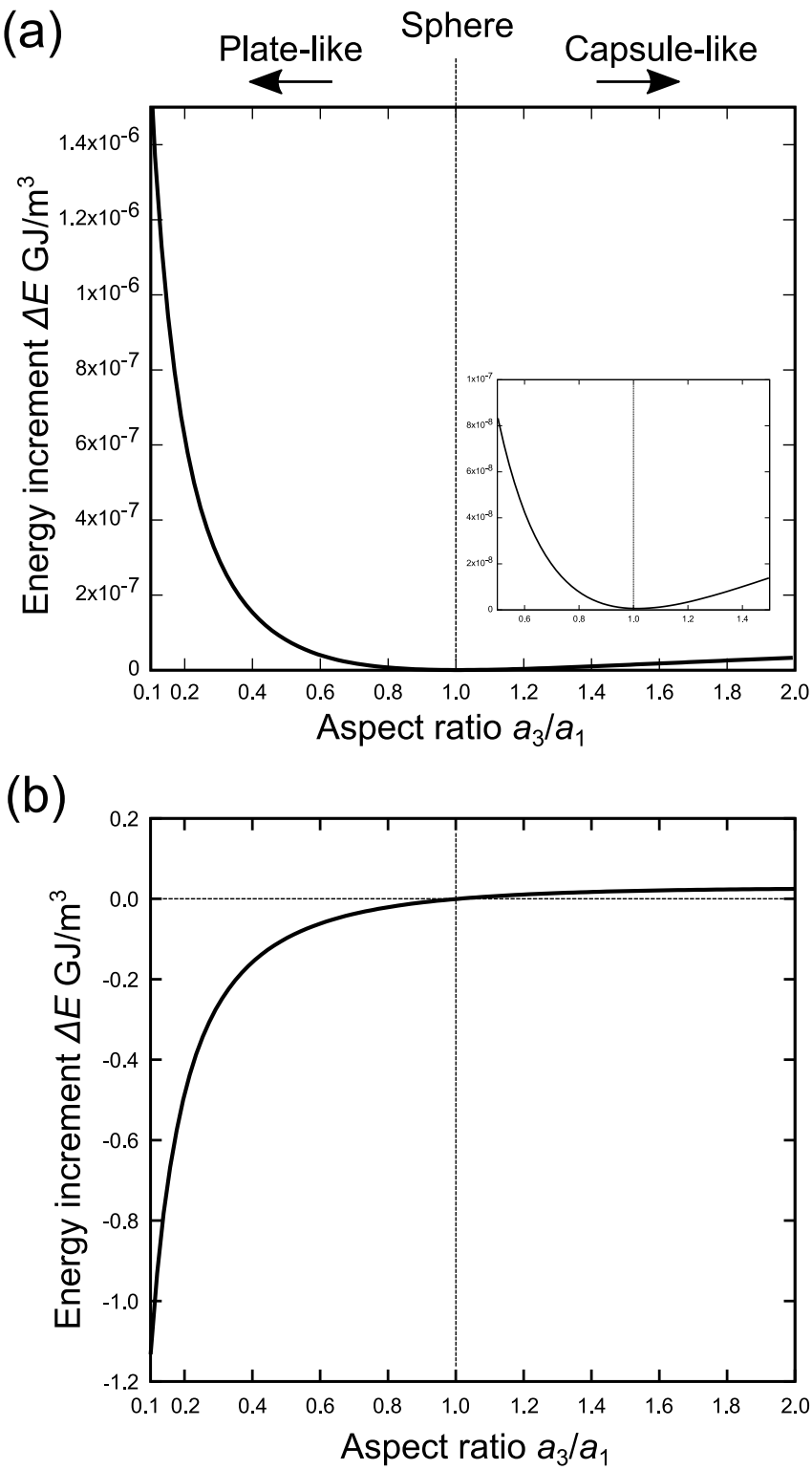

Fig. 11. Aspect ratio $\frac{a_3}{a_1}\left(=\frac{a_3}{a_2}\right)$ of ellipsoidal hydrogen blister vs ΔE plot for (a) 4 N and (b) 2 N samples. The lowest value of ΔE is at $\frac{a_3}{a_1}=1.0$ for 4 N (sphere) and $\frac{a_3}{a_1}=0.1$ for 2 N (plate-like), respectively.

lowest ΔE, for 2 N blister, plate-like shape $\left(\frac{a_3}{a_1}=0.1\right)$, which is the lowest aspect ratio, have the lowest ΔE. This is fairly consistent with the experimental observation; thus, it is theoretically confirmed that the shape change is due to the local stress of the precipitates. Moreover, the shape of the blister is determined by the competition between the gas pressure in the blister and the local stress of the precipitates; hydrogen gas pressure drives the blister shape to a sphere and the local stress of precipitates drives it to a penny (we confirmed this is mainly due to large σ_{33} of plate-like Si). Because the gas pressure in the blister is at the MPa level, which is quite small compared with the GPa-level local stress due to the precipitates, the local stress is the dominant factor affecting the blister shape. Notably, $\left(\frac{a_3}{a_1}=0.1\right)$ is not the minimum for the 2 N case

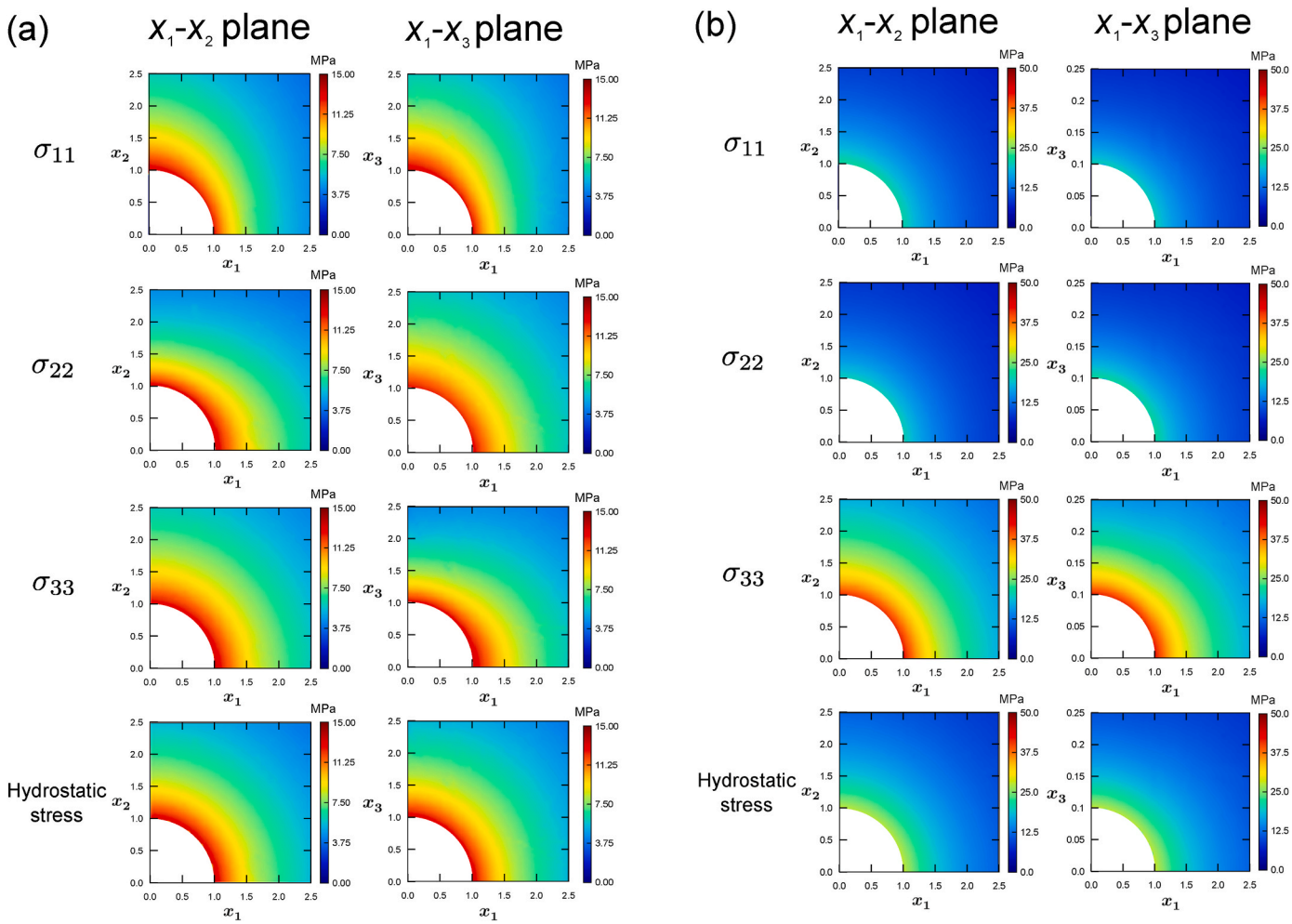

Fig. 12. Local stress fields around the hydrogen blisters. (a) Spherical blister (for 4 N: $a_1 = a_2 = a_3 = 1.0, P = 5.24$ MPa) and (b) plate-like blister (for 2 N: $a_1 = a_2 = 1.0, a_3 = 0.1, P = 2.23$ MPa). Notably, $\sigma_{23}(\boldsymbol{x}) = \sigma_{31}(\boldsymbol{x}) = \sigma_{12}(\boldsymbol{x}) = 0$. The stress fields inside the ellipsoid are omitted.

from the slope of the curve in Fig. 11; thus, a thin plate-like blister may be favored theoretically, although it is not investigated.

We also calculated the local stress field around the blisters using equation (4) for the 4 N sphere and 2 N optimal ellipsoidal blister (plate-like); the results are shown in Fig. 12. Around the spherical blister (4 N), approximately 15 MPa of normal stress, which is approximately 3 times larger than the gas pressure, is induced by the blister. Additionally, around the plate-like blister (2 N), interestingly at the edge of the longitude, approximately 50 MPa σ_{33} normal stress is induced by the blister, which is approximately 25 times larger than the gas pressure. This indicates that the plate-like blister plays an important role in hydrogen embrittlement, the large local normal stress at the edge of the blister drives the hydrogen concentration around it and the longitudinal growth of the blister, which is consistent with our experimental observation in previous section; the size of blisters in 2 N is larger than that in 4 N, and eventually resulting in cracking. Thus, our results suggest that understanding and controlling blister shape are important for preventing hydrogen embrittlement.

5. Summary

This study explored the effect of purity of aluminum on the morphology of blisters formed on aluminum plates. The study findings reveal that the shape and number density of the blisters varied according to the purity of the aluminum. Spherical blisters were observed in high-purity aluminum (99.99 %; 4N), compared to low-purity aluminum (99 %; 2N). This morphological change may be due to the local stress caused by neighboring impurity precipitates; this was theoretically verified through Eshelby's ellipsoidal inclusion analysis. Note that although the number of blisters were lower in 2N than in 4N, the size of the blisters were larger, suggesting that hydrogen embrittlement effects were significant in low-purity aluminum.

CRediT authorship contribution statement

Keitaro Horikawa: Writing – original draft. **Akio Ishii:** Writing – review & editing, Methodology.

Declaration of competing interest

The authors declare that they have no known competing financial interests or personal relationships that could have appeared to influence the work reported in this paper.

Data availability

Data will be made available on request.

Acknowledgements

This study was partially supported by a Grant-in-Aid for Scientific Research (C) 21K03771, (B)21H01604 from the Japan Society for the

Promotion of Science (JSPS). K. H. acknowledges the partial financial support by The Light Metal Educational Foundation, Inc. in Osaka, Japan.

References

[1] K. Horikawa, M. Taniyama, H. Kobayashi, Morphological observation of blisters generated in a high purity aluminum plate, J. Jpn. Inst. Light Metals 70 (2020) 432–434, https://doi.org/10.2464/jilm.70.432 (in Japanese).
[2] T. Ohnishi, Hydrogen in pure aluminum and in aluminum alloys, J. Jpn. Inst. Light Metals 39 (1989) 235–251, https://doi.org/10.2464/jilm.39.235 (in Japanese).
[3] K. Horikawa, Current research trends in aluminum alloys for a high-pressure hydrogen gas container, J. Jpn. Inst. Light Metals 60 (2010) 542–547, https://doi.org/10.2464/jilm.60.542 (in Japanese).
[4] N. Kawashima, H. Yamada, Y. Sato, Study on the blistering of aluminium (1st Report), J. Jpn. Inst. Light Metals 13 (1963) 231–236, https://doi.org/10.2464/jilm.13.231 (in Japanese).
[5] N. Kawashima, H. Yamada, Y. Sato, Study on the blistering of aluminium (2nd Report), J. Jpn. Inst. Light Metals 13 (1963) 307–314, https://doi.org/10.2464/jilm.13.307 (in Japanese).
[6] H. Umeda, G. Itoh, Y. Kato, Effect of heat treatment condition on the hydrogen content in Al-4%Mg alloys, J. Jpn. Inst. Light Metals 56 (2006) 203–209, https://doi.org/10.2464/jilm.56.203 (in Japanese).
[7] H. Umeda, G. Itoh, Y. Kato, Effect of alloying elements on the change of hydrogen content in Al-Mg alloys during annealing, J. Jpn. Inst. Light Metals 56 (2006) 423–428, https://doi.org/10.2464/jilm.56.423 (in Japanese).
[8] K. Horikawa, Quantitative monitoring of the environmental hydrogen embrittlement of Al-Zn-Mg-based aluminum alloys via dynamic hydrogen detection and digital image correlation, Scripta Mater. 199 (2021) 113853, https://doi.org/10.1016/j.scriptamat.2021.113853.
[9] H. Yamada, M. Tsurudome, N. Miura, K. Horikawa, N. Ogasawara, Ductility loss of 7075 aluminum alloys affected by interaction of hydrogen, fatigue deformation, and strain rate, Mater. Sci. Eng. 642 (2015) 194–293, https://doi.org/10.1016/j.msea.2015.06.084.
[10] K. Horikawa, M. Arayama, H. Kobayashi, Quantitative detection of hydrogen gas release during slow strain rate testing in aluminum alloys, Mater. Sci. Forum 1016 (2021) 568–573. https://doi.org/10.4028/www.scientific.net/MSF.1016.568.
[11] K. Horikawa, H. Kobayashi, Hydrogen absorption of pure aluminum by friction of the surface in water and its effect on tensile properties, J. Japan Inst. Metals 84 (2020) 68–73, https://doi.org/10.2320/jinstmet.JB201903 (in Japanese).
[12] K. Horikawa, H. Kobayashi, Hydrogen charging of aluminum using friction in water, J. Vis. Exp. 155 (2020) e60711, https://doi.org/10.3791/60711.
[13] K. Horikawa, T. Matsubara, H. Kobayashi, Hydrogen charging of Al–Mg–Si-based alloys by friction in water and its effect on tensile properties, Mater. Sci. Eng. 764 (2019) 138199, https://doi.org/10.1016/j.msea.2019.138199.
[14] H. Kostron, Aluminium und Gas II. Blasen und Poren im Knetmaterial, Int. J. Mater. Res. 43 (1952) 373–387, https://doi.org/10.1515/ijmr-1952-431101 (in German).
[15] Y. Ueda, T. Funabiki, T. Shimada, K. Fukumoto, H. Kurishita, M. Nishikawa, Hydrogen blister formation and cracking behavior for various tungsten materials, J. Nucl. Mater. (2005) 337–339, https://doi.org/10.1016/j.jnucmat.2004.10.077, 1010–1014.
[16] T. Funabiki, T. Shimada, Y. Ueda, M. Nishikawa, Effect of tungsten microstructure on blister formation by hydrogen and carbon mixed ion beam irradiation, J. Nucl. Mater. (2004) 329–333, https://doi.org/10.1016/j.jnucmat.2004.04.174, 780–784.
[17] H.A. Wriedt, R.A. Oriani, Effect of tensile and compressive elastic stress on equilibrium hydrogen solubility in a solid, Acta Metall. 18 (1970) 753–760, https://doi.org/10.1016/0001-6160(70)90039-8.
[18] T. Mura, Micromechanics of Defects in Solids, Martinus-Nijhoff Publishers, Boston, 1987.
[19] T. Mura, P.C. Cheng, The elastic field outside an ellipsoidal inclusion, J. Appl. Mech. 44 (1977) 591–594, https://doi.org/10.1115/1.3424141.
[20] A. Ishii, Ab initio morphology prediction of Zr hydride precipitates using atomistically informed Eshelby's ellipsoidal inclusion, Comput. Mater. Sci. 211 (2022) 111500, https://doi.org/10.1016/j.commatsci.2022.111500.
[21] A. Ishii, Morphology prediction of elastically interacting Zr hydride precipitates and cracks in α-Zr using atomistically informed Eshelby's ellipsoidal inclusion, Comput. Mater. Sci. 231 (2024) 112568, https://doi.org/10.1016/j.commatsci.2023.112568.
[22] J.D. Eshelby, The determination of the elastic field of an ellipsoidal inclusion, and related problems, Proc. R. Soc. Lond. Ser. A Math. Phys. Eng. Sci. 241 (1957) 376–396.
[23] J.D. Eshelby, Elastic inclusions and inhomogeneities, Prog. sol. mech. 2 (1961) 89–140.
[24] A. Ishii, Influence of elastic anisotropy on the shapes of ellipsoidal blisters and stress field around the blisters in solid materials, AIP advance 13 (2023) 125024, https://doi.org/10.1063/5.0182632.
[25] N. Kinoshita, T. Mura, Elastic fields of inclusions in anisotropic media, Phys. Status Solidi 5 (1971) 759–768, https://doi.org/10.1002/pssa.2210050332 (a).
[26] A. Jain, S.P. Ong, G. Hautier, W. Chen, W.D. Richards, S. Dacek, S. Cholia, D. Gunter, D. Skinner, G. Ceder, K.A. Persson, Commentary: the materials project: a materials genome approach to accelerating materials innovation, Apl. Mater. 1 (2013) 011002, https://doi.org/10.1063/1.4812323.
[27] M. Liu, R. Zheng, W. Xiao, X. Yu, Q. Peng, C. Ma, Concurrent enhancement of strength and ductility for Al-Si binary alloy by refining Si phase to nanoscale, Mater. Sci. Eng. 751 (2019) 303–310, https://doi.org/10.1016/j.msea.2019.02.081.
[28] W. Wu, M. Gong, B. Wei, A. Misra, J. Wang, Atomistic modeling of interface strengthening in Al-Si eutectic alloys, Acta Mater. 225 (2022) 117586, https://doi.org/10.1016/j.actamat.2021.117586.
[29] K. Kaneko, R. Nagayama, K. Inoke, E. Noguchi, Z. Horita, Application of three-dimensional electron tomography using bright-field imaging—two types of Si-phases in Al–Si alloy, Sci. Technol. Adv. Mater. 7 (2006) 726–731, https://doi.org/10.1016/j.stam.2006.06.006.